# A COLOR-TEMPERATURE BASED METHOD TO RECOVER THE SPECTRAL INFORMATION OF THE SHADED OBJECTS

Gongqi Zhou[1], Qiming Qin[2] and Zihua Wu[3]

[1]Institute of Remote Sensing and Geographic Information System (IRSGIS), Peking University, No.5 Yihuyuan Road Haidian District, Beijing, P.R.China 100871, Email: zhougq@pku.edu.cn

[2]Institute of Remote Sensing and Geographic Information System (IRSGIS), Peking University, No.5 Yihuyuan Road Haidian District, Beijing, P.R.China 100871, Email: qmqin@pku.edu.cn

[3]Institute of Remote Sensing and Geographic Information System (IRSGIS), Peking University, No.5 Yihuyuan Road Haidian District, Beijing, P.R.China 100871, Email: qqbbnease1004@126.com

## KEYWORDS:

Fractional vegetation cover; Color-temperature; Image processing; Shadow removing

## ABSTRACT:

A color-temperature based projection method in log-spectral space called Color-Temperature-based Mapping on Maximum Illuminated Objects (CTMMIO), which describe solar incident radiation as a function of color temperature to avoid the large calculation work in atmosphere simulation and correction, was built to recover the information in shadow area in high-resolution satellite imageries. Simulations of surface incident radiance and correlated black body radiation using MODTRAN(MODerate resolution atmospheric TRANsmission) software shows that CTMMIO can recover the light condition of shadowed object from the diffuse skylight into a direct illuminated situation. The experiment on the Chinese GaoFen-series(GF) high resolution image shows that in the shorter wavelength band, the reflectance difference brought by sky diffused radiation spectrum in shadow area is restored to the level of normal light condition at the cost of one band's information. The normalized difference vegetation index (NDVI) of forest area is also enhanced, and then improve the accuracy of vegetation fractional cover(FVC) estimation. Comparison between illuminated area and shadowed area shows that the vegetation cover estimated after CTMMIO increased about 0.23, close to its well-illuminated condition. As a result, this method could help enhance the homogeneity of the same ground objects, the precision of the ground parameter inversion such as vegetation cover could be improved remarkably.

## 1. INTRODUCTION

As the high-resolution remote sensing has been widely applied in earth observation applications, it also encountered many challenges. One of the challenges is the removal of spectral heterogeneity, which is often caused by shadow, from the same object. The mutual shadowing effect between ground objects are more pronounced in the image as the resolution increases, meaning that the proportion of pure-shadow pixels has increased. The NDVI and its derivative products, such as leaf area index, fractional vegetation cover(FVC) and other indices are suffered from the shadow. The NDVI error could be 13.5% due to topographic shadow effects(Burgess, Lewis et al. 1995), and other research showed the same results by Kusaka et al(Kusaka, Kurokawa et al. 1997). Asner found that the canopy mutual shading can cause 25%±12% amount of pixels covered by shadow in forest, and about 30%~50% of the band variance is caused by shadow(Asner and Warner 2003). The intrinsic spectral information in shadow area is essential to the

high-resolution imageries in removing the effect of synonyms spectrum(Fahsi, Tsegaye et al. 2000).

The algorithm of extraction the intrinsic spectral information from the shadowed ground objects has developed in many remote sensing applications, such as experience model(Colby 1991, Chen, Wen et al. 2007), semi-experience model(Teillet, Guindon et al. 1982, Gu and Gillespie 1998, Soenen, Peddle et al. 2008), time-series composition(Arellano 2003, Roy, Ju et al. 2008), and color-invariant method(Makarau, Richter et al. 2011, Corke, Paul et al. 2013). The shadow caused by cloud or terrain can be removed by atmosphere correction or topography correction, however these methods rely on the input of digital elevation model(DEM)(Saha, Arora et al. 2005, Richter and Schlapfer 2012) and ground bidirectional reflectance parameters(bidirectional reflectance distribution function, BRDF), and are not suitable for high-resolution images. The shadow area in image always shows an over-corrected or under-corrected result, thus affect the vegetation indices(VIs)(Panneton and Brouillard 2009).

To eliminate the shadow effects on VIs, this paper proposed a method named Color-Temperature-based Mapping on Maximum Illuminated Objects(CTMMIO) based on color-invariant method, aimed at recovering the illumination information in shadow area using black-body scatter feature when the atmosphere condition and surface BRDF are unknown. A shadow-free color log-space model is proposed, which allows projection to a max-illuminated plane in log-spectral-space and, eliminates the extra radiance brought by scatter light. Because CTMMIO method only use color-temperature as a simulation factor of surface radiance, the calculation efficiency is improved as the atmosphere parameters and surface BRDF modelling and estimation are reduced, and the accuracy of VIs is improved.

## 2. METHOD

The Plank's Law of black-body can be expressed as:

$$E(\lambda,T)=\frac{2hc^2}{\lambda^5}\frac{1}{e^{\frac{hc}{\lambda k_B T}}-1} \tag{1}$$

Where c is the speed of light, h is the Plank constant, $k_B$ is Boltzmann constant, T is temperature, $\lambda$ is the wavelength. When light source emits radiance, if the irradiance is similar to the black body at temperature $T_B$, we mark $T_B$ as the correlated color temperature(CCT), the color temperature of this object $T_C=T_B$. A coefficient $k_{CCT}$ is needed because the concept of CCT is only referred to descript the shape of irradiance spectral but not the magnitude.

$$E(\lambda,T)=k_{CCT}E(\lambda,T_B) \tag{2}$$

where $k_{CCT}$ is the conversion coefficient of actual spectral radiance.

Suppose the color temperature T is invariable then the sensor is imaging, and the surface is Lambertian, then the sensor response $R_k$ at kth band can be expressed as:

$$R_k=\sigma\int E(\lambda)\rho(\lambda)Q_k(\lambda)\mathrm{d}\lambda \tag{3}$$

where $Q_k(\lambda)$ is the spectral response function(SRF) at kth band, $E(\lambda)$ is the incident radiance, $\rho(\lambda)$ is the intrinsic reflectance, $\sigma$ is the constant of incident angle. Consider the extreme condition of a narrow SRF:

$$Q_k(\lambda)=q_k\delta(\lambda-\lambda_k) \tag{4}$$

Plank's formula can be written as:

$$E(\lambda,T)=\sigma\frac{2hc^2}{\lambda^5(e^{hc/k_B\lambda T}-1)}\rho(\lambda)q_k \tag{5}$$

As the $e^{hc/k_B\lambda T}$ is much greater than 1 under 10000K, the -1 term can be neglected for a simpler expression of plank's formula according to Wien's Law:

$$E(\lambda,T)\approx\sigma\frac{2hc^2}{\lambda^5 e^{hc/k_B\lambda T}}\rho(\lambda)q_k \tag{6}$$

There are 4-7 or even more bands for satellite or aerial based sensors. Select one band p as the base band, the ratio between each band *k* and *p* are calculated, and noted as $\chi$ :

$$\chi_j=\frac{R_k}{R_p}, k\in\{1,2,...,n_{bands}\}, k\neq p,\ j\in\{1,2,...,n_{bands}-1\} \tag{7}$$

where $n_{bands}$ is the number of sensor bands. So,

$$\chi_j=\frac{\sigma\frac{2hc^2}{\lambda_k{}^5 e^{hc/k_B\lambda_k T}}\rho(\lambda_k)q_k}{\sigma\frac{2hc^2}{\lambda_p{}^5 e^{hc/k_B\lambda_p T}}\rho(\lambda_p)q_k} \tag{8}$$

The logarithmic form of the above formula can be written as:

$$\chi_j'=\ln\chi_j=\ln(\frac{s_k}{s_p})+\frac{1}{T}(e_k-e_p) \tag{9}$$

where $s_k=\lambda_k^{-5}\rho(\lambda_k)q_k$, $e_k=-hc/k_B\lambda_k$. It can also be written in vector form:

$$\boldsymbol{\chi}'=\mathbf{s}+\frac{1}{T}\mathbf{e} \tag{10}$$

where **s** is a 2-dimentional vector related to only to object's intrinsic reflectance and SRF, and is independence with incident radiance. **e** is also a 2-dimentional vector is related to sensor's bands, and is independent with object's intrinsic reflectance(Finlayson, Hordley et al. 2006). $\boldsymbol{\chi}'$ moves along a straight line in logarithmic space when T varies. This logarithmic space is denoted by log-spectral space (shown in fig. 1). The direction of vector e is also depending on sensor's bands. When CCT changes, the point in log-spectral space will move along with e direction. In practical applications, the band *p* can be replaced with the geometric mean of all bands *G*(Finlayson, Hordley et al. 2006, Corke, Paul et al. 2013).

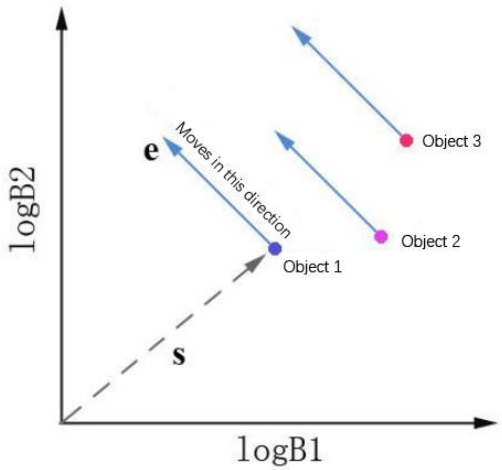


Figure 1. The illustration of linear relationship in log-spectral space (2-D). B1 and B2 are two bands in the image.

The above derivation is based on the hypothesis of narrow SRFs. The overlap between SRFs will lead a failure of the above formulas. For satellite sensors, the shape of SRFs is regular, and the overlap of SRFs is very small that can be neglected. According to researches and simulations using selected satellite's SRFs, the log-spectral space method is still valid in well calibrated satellites(Corke, Paul et al. 2013, Romero and Leus 2013).

The incident spectral radiance shape at ground level can be described by black body irradiance and coefficient $k_B$. In other word, the spectral emit by black body of a different CCT can be used to depict the different incident illumination conditions, which includes straight illumination, scatter illumination and a mixture of straight and scatter illumination. According to the research of Makarau(Makarau, Richter et al. 2011), the CCT of sunny condition is approximately 5500K to 6500K, the CCT of scatter light (the blueish sky light scattered by atmosphere molecular) is about 7500K~10000K according to different atmosphere conditions(Judd, MacAdam et al. 1964, Tian, Zhu et al. 2012).

The red and NIR bands are mostly used in vegetation recognition applications, and is related to many VIs. The blue band strongly influenced by atmosphere scattering and absorption and its SRF overlaps with green band SRF, so it will not be considered in this paper to avoid the failure of independent SRF condition. The red, green and near-infrared bands are noted as R, G, and NIR correspondingly, and the logarithmic form of each band is noted as logR, logG and logNIR. Because of the use of geometric mean of the 3 selected bands, in the 3-dimentional log-space made up of lofR, logG and logNIR, the scatter points of an image are distributed on a plain passing through the point (0,0,0). The actual information carried by scatter points is 2-dimentionally, so only two end-members are enough to determine the maximum illuminated plain(line). Assuming there are only two kinds of ground types: vegetation and non-vegetation(bare-land), the end-members should be pure vegetation and pure bare land. For shadow pixels, by projecting along the **e** direction, the cross point of maximum illumination line and the extension of vector e will be the real reflectance under maximum illumination (well illuminated with a lower CCT).

## 3. DATA AND PREPROCESS

### 3.1. GF-2 High-Resolution Data

GF-2(GaoFen -2) is a high-resolution satellite launched by China aimed at providing finer resolution for agriculture, forestry and urban researches. The PMS sensor provides 1-meter panchromatic (0.8 meter at nadir), 4-meter multi-spectral images. The information of PMS sensor is described in the form below:

Table 1 GF-2 PMS parameters

| band | Wavelength (μm) | Space | Detection | Side angle | Revisit |
|---|---|---|---|---|---|

| | | | resolution | width | | period |
|---|---|---|---|---|---|---|
| **PMS-2** | pan | 0.45-0.90 | 1m | 45km | ±35° | 5d |
| | 1 | 0.45-0.52 | 4m | 45km | ±35° | 5d |
| | 2 | 0.52-0.59 | 4m | 45km | ±35° | 5d |
| | 3 | 0.63-0.69 | 4m | 45km | ±35° | 5d |
| | 4 | 0.77-0.89 | 4m | 45km | ±35° | 5d |

The research area is set at Huoshan county, Anhui province, between 115.9E to 116.2E, 31.4N to 31.6N. image acquire time is 26th April, 2015. The main shadow type is cloud shadow. the DN number was calibrated and converted to ground upward radiance using MODTRAN software. The ground upward radiance image is shown below:

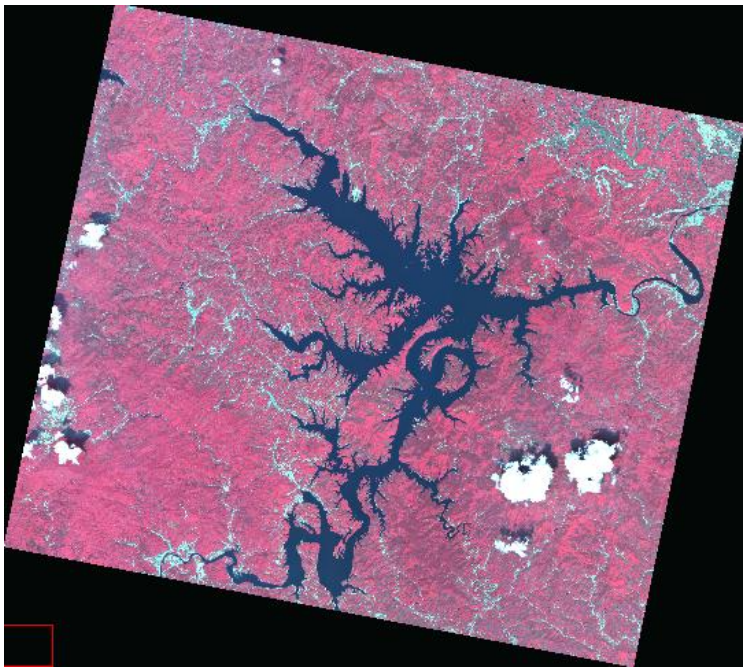

Figure 2. The ground upward radiance image after correction in MODTRAN.

Cloud and water body pixels are masked using the algorithm developed by Zhu et al(Zhu and Woodcock 2012), as we only concern vegetation and bare land in this paper for FVC estimation,

## 3.2. End-Member Selection

End-member can be considered as the pure pixel in an image. The selection of end-member is significant to the projection procedure and thus affect the final results. For FVC estimation, two end-members (vegetation and soil) are needed in this paper. PPI(pixel purity index) method in ENVI software is employed to select end-members. The selected end-members' reflectance is shown in table 2:

Table 2 GF-2 end-members

| **End-member** | **Band1 reflectance** | **Band2 reflectance** | **Band3 reflectance** | **Band4 reflectance** |
|---|---|---|---|---|
| **Vegetation** | 0.0860 | 0.1103 | 0.0847 | 0.5105 |
| **Soil** | 0.1923 | 0.2345 | 0.2896 | 0.3972 |

### 3.3. Estimation of Projection Vector and The Color-Temperature Invariant Image

The project vector **e** is only connected to sensor's SRF, and its direction is invariant with CCT. By select region of interests (ROIs) of same object with two different illumination conditions, vector **e** can be estimated by subtract the mean of light ROI $P_{light}$ with the mean of shadow ROI $P_{shadow}$.

$$\mathbf{e} = P_{light} - P_{shadow}$$

The projection vector e is calculated through two small ROIs at the edge of cloud shadow, and the result is (-0.215, -0.0538, 0.2552). mark $P_{proj}$ as the cross point of the extension line of vector e and the maximum illuminated line, then the projected new pixel value can be expressed as:

$$P_p(band_i) = Ge^{P_{proj}(band_i)}$$

Where $band_i$ is the coordinates of ith band, and $P_p$ is the new pixel radiance after CTMMIO projection, G is the geometric mean of all bands. The simulation of different types of ground objects of GF-2 under different CCTs, and the scatter points of ROIs of the image in log-spectral are plotted in figure 2.

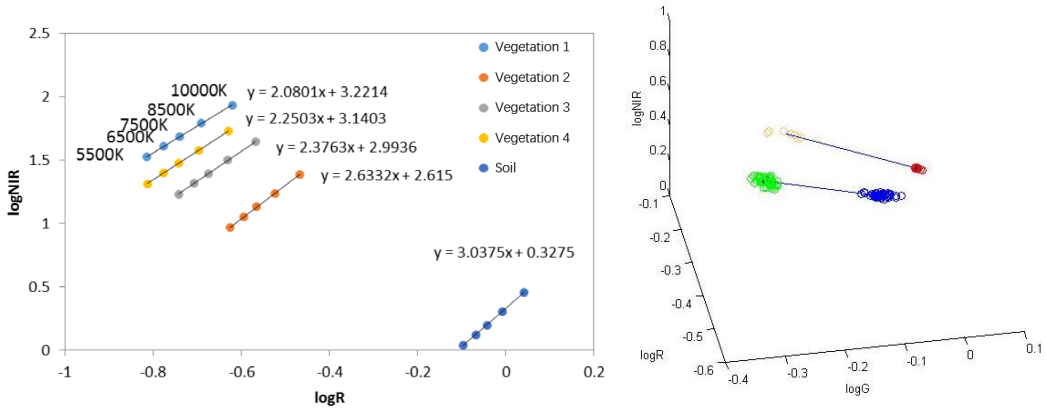


Figure 3. The illustration of log-spectral space. The left one is 2-D log-spectral space built by logB and logNIR, showing that the maximum illumination plain(line) and how CCT impacts the scatter point in log-spectral space. The response of all types of GF-2 under different CCTs are simulated using eq. (1) with MODTRAN software; the right one is 3-D log-spectral space built by logR, logG, and logNIR. The red and blue points are scatter from shadow soil and shadow vegetation ROIs, and the yellow and green ones for illuminated ROIs respectively. The blue line is the projection vector **e**.

## 4. RESULTS AND DISCUSSION

The projected image is shown as below (only part of image is exhibited where shadow appears):

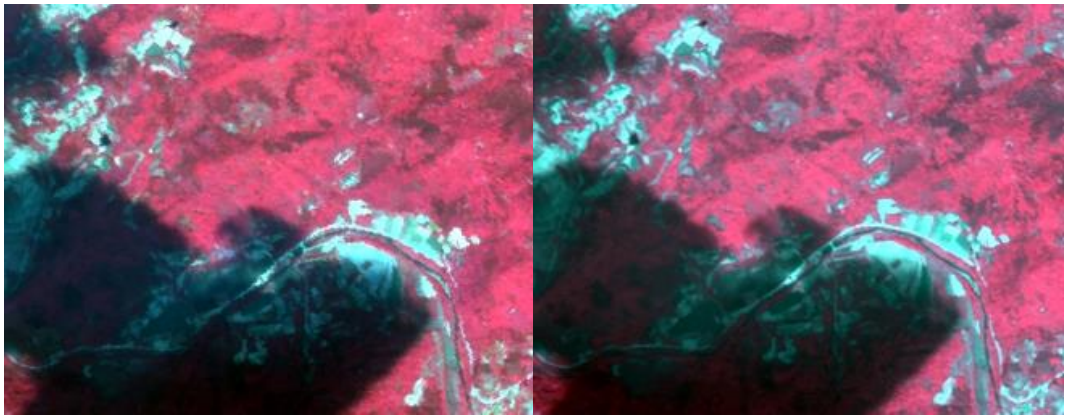

Figure 4. The comparison of one shadowed area in GF-2 image. Left one is original image from fig.2; and the right one is the result after CTMMIO projection.

As can be seen from fig. 4, the shadow area shows a slightly difference in shadow area, because CTMMIO method adjusts the radiance spectral shape but not the magnitude of radiance. To illustrate the enhancements in shadow area, NDVI was selected as an indicator to check the consistency at the edge of shadows, for its ability to resist some of the shadow effect. The NDVI of both projected and un-projected images was calculated to compare the shadow impact for NDVI.

Figure 5. The NDVI results of fig. 4.

As can be seen from fig.5, the NDVI still suffers from the shadowing effect, and appears to be much lower compare to that of the well illuminated area.

The pixel dichotomy model was selected to estimate the FVC with two thresholds of NDVI at the place of 5% and 95% of accumulated NDVI histogram. Note $NDVI_{CT}$ as the NDVI value after CTMMIO projection, and $NDVI_{ref}$ as the NDVI directly calculated from the ground reflectance image after FLAASH atmosphere correction in ENVI software. The lower and upper threshold of $NDVI_{CT}$ and $NDVI_{ref}$ are (0.206, 0.660) and (0.288, 0.720). then FVC images were calculated separately using pixel dichotomy method:

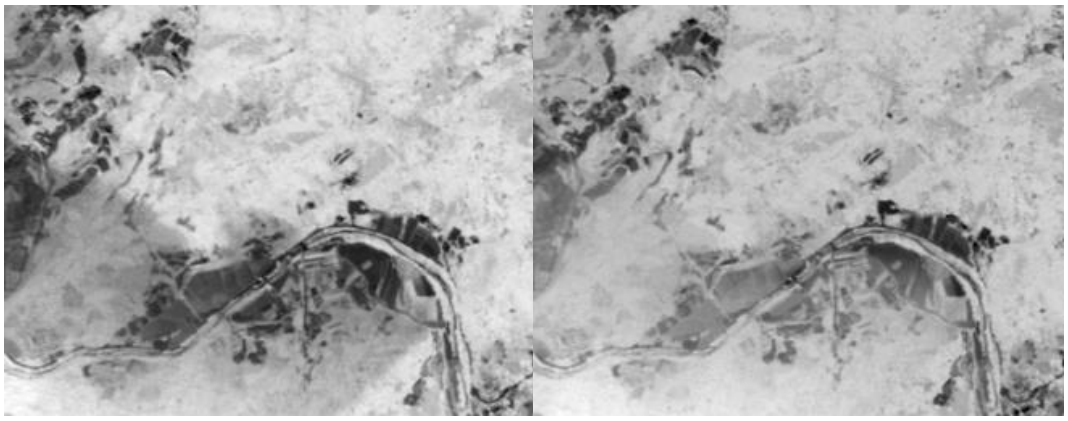

Figure 6. The NDVI results. Left one is $NDVI_{ref}$; right one is $NDVI_{CT}$.

To emphasize the improvements of CTMMIO projection, we applied another projection in RGB color space to enhance the intensity of pseudo-color image composed by NIR, R and G band. Being similar to CTMMIO, the intensity enhancement projection use 3end-members to define a maximum illuminated plain in RGB color space, and project each pixel's scatter points onto the maximum illuminated plain. It is helpful to improve the brightness (magnitude of radiance in this paper) of dark area and makes the visual interpretation easier.

The image after intensity enhancement projection is shown as below:

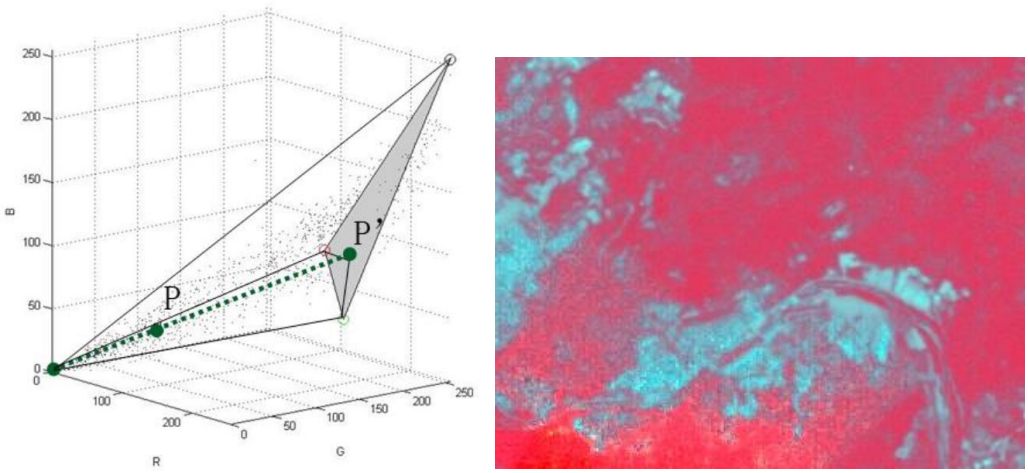


Figure 7. The illustration of brightness enhance projection(left) and its result(right), where P is a random pixel in image, and P'is the projected point in maximum illumination plain in RGB color space(for demonstration, it can be any n bands of an multi-spectral image). The maximum illumination plain is defined by 3 end-members(colored hollow circles in the left figure).

As shown in fig.7, the shadow margin is hard to be seen in projected image, and the color in the image is brighter. The brightness and spectral shape (color) of the shadow area is similar to that of the illuminated area, including the shadow area that caused by topographic at the upright corner of the image, and the two different vegetation types (in two different red colors) was well kept. However, there is mosaic effects in shadow area after projection because of the low signal-noise-ratio(SNR).

Assuming that the atmosphere corrected GF-2 image has a relatively accurate ground reflectance in illuminated area, we can validate the FVC of the projected image to evaluate the effectiveness of CTMMIO method. 2 ROIs of illuminated area and shadowed area were selected at the edge of shadow, where was considered to be similar at ground. The FVC of each ROI was calculated by pixel dichotomy method in both projected image and atmosphere corrected image. The ROIs in image is shown in fig 8(left), and the FVC scatter point figure is shown in fig 8(right).

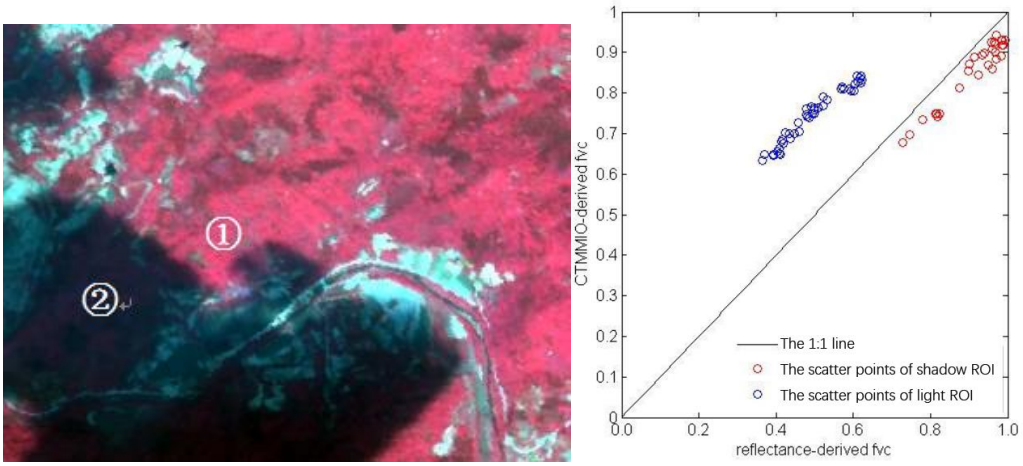


Figure 8. The ROIs in GF-2 image (left); and the FVC scatter points of 2 ROIs (right).

Fig.8 shows that there is little change of FVC in illuminated area, but the projected FVC is a bit lower than atmosphere corrected FVC. For illuminated area, the coverage of dense vegetation is large, which makes the 95% percentage NDVI number is larger than the actual full-cover value, therefore makes the difference of projected FVC. However, the difference is quite small so it can be considered the same after projection. The main difference appears in shadow area, where CTMMIO derived FVC is much higher than reflectance derived FVC. Assuming these two ROIs are of the same type of ground cover, their FVCs should be the same or similar, however the existence of shadow

brought down the FVC in shadow area by about 0.23 (blue points in fig. 8(right)). The CTMMIO method has brought the underestimated FVC in shadow area to its theoretical level. The level of FVC in shadow area has adjusted to be equal to that of in illuminated area.

## 5. CONCLUSION

This paper proposed a method called CTMMIO based on the concept of color temperature, which has been applied to the FVC estimation and vegetation information extraction in high-resolution image GF-2. The results showed that the spectral difference caused by CCT was the main reason for the effect of shadow, and CTMMIO method can adjust the illumination spectral shape to a normal lighting condition which include direct and diffuse illumination and has a lower CCT. The intrinsic variance of ground objects is decreased and the NDVI has also improved. For pixel dichotomy model in FVC estimating, CTMMIO method can be a good means to remove the shadow impact on satellite images without knowing ground BRDF. Due to the limitation of the quantity of images of GF-2, the remove of other shadow types are not carried out, and more tests are needed under other scenes, such as the mutual shadowing in urban and topographic shadow in mountainous area.

## REFERENCE:


Arellano, P. (2003). "Missing information in remote sensing: wavelet approach to detect and remove clouds and their shadows." International Institute for Geo-Information Science and Earth Observation, Enschede, The Netherlands.

Asner, G. P. and A. S. Warner (2003). "Canopy shadow in IKONOS satellite observations of tropical forests and savannas." Remote Sensing of Environment **87**(4): 521-533.

Burgess, D. W., P. Lewis and J. P. A. L. Muller (1995). "Topographic effects in AVHRR NDVI data ☆." Remote Sensing of Environment **54**(3): 223-232.

Chen, Y., D. Wen, L. Jing and P. Shi (2007). "Shadow information recovery in urban areas from very high resolution satellite imagery." International Journal of Remote Sensing **28**(15): 3249-3254.

Colby, J. D. (1991). "Topographic normalization in rugged terrain." Photogrammetric Engineering and Remote Sensing **57**(5): 531-537.

Corke, P., R. Paul, W. Churchill and P. Newman (2013). "Dealing with Shadows: Capturing Intrinsic Scene Appearance for Image-based Outdoor Localisation." 2013 Ieee/Rsj International Conference on Intelligent Robots And Systems (Iros): 2085-2092.

Fahsi, A., T. Tsegaye, W. Tadesse and T. Coleman (2000). "Incorporation of digital elevation models with Landsat-TM data to improve land cover classification accuracy." Forest Ecology & Management **128**(s 1–2): 57-64.

Finlayson, G. D., S. D. Hordley, C. Lu and M. S. Drew (2006). "On the removal of shadows from images." IEEE Transactions on Pattern Analysis & Machine Intelligence **28**(1): 59-68.

Gu, D. and A. Gillespie (1998). "Topographic normalization of Landsat TM images of forest based on subpixel sun–canopy–sensor geometry." Remote sensing of Environment **64**(2): 166-175.

Judd, D. B., D. L. MacAdam, G. Wyszecki, H. Budde, H. Condit, S. Henderson and J. Simonds (1964). "Spectral distribution of typical daylight as a function of correlated color temperature." Josa **54**(8): 1031-1040.

Kusaka, T., T. Kurokawa, M. Hojo and S. Ochiai (1997). "Finite Element Simulation of Impact End Notched Flexure Test Using Ramped Incident Waves : Verification of the Proposed Method for Estimating Energy Release Rate." Nihon Kikai Gakkai Ronbunshu A Hen/transactions of the Japan Society of Mechanical Engineers Part A **63**(605): 158-164.

Makarau, A., R. Richter, R. Müller and P. Reinartz (2011). "Adaptive shadow detection using a blackbody radiator model." Geoscience and Remote Sensing, IEEE Transactions on **49**(6): 2049-2059.

Panneton, B. and M. Brouillard (2009). "Colour representation methods for segmentation of vegetation in photographs." Biosystems Engineering **102**(4): 365-378.

Richter, R. and D. Schlapfer (2012). "Atmospheric/topographic correction for airborne imagery: ATCOR-4 User Guide." DLR IB: 565-502.

Romero, D. and G. Leus (2013). "Wideband spectrum sensing from compressed measurements using spectral prior information." IEEE Transactions on Signal Processing **61**(24): 6232-6246.

Roy, D. P., J. Ju, P. Lewis, C. Schaaf, F. Gao, M. Hansen and E. Lindquist (2008). "Multi-temporal MODIS–Landsat data fusion for relative radiometric normalization, gap filling, and prediction of Landsat data." Remote Sensing of Environment **112**(6): 3112-3130.

Saha, A. K., M. K. Arora, E. Csaplovics and R. P. Gupta (2005). "Land Cover Classification Using IRS LISS III Image and DEM in a Rugged Terrain: A Case Study in Himalayas." Geocarto International **20**(2): 33-40.

Soenen, S., D. Peddle, C. Coburn, R. Hall and F. Hall (2008). "Improved topographic correction of forest image data using a 3 - D canopy reflectance model in multiple forward mode." International Journal of Remote Sensing **29**(4): 1007-1027.

Teillet, P. M., B. Guindon and D. G. Goodenough (1982). "On the Slope-Aspect Correction of Multispectral Scanner Data." Canadian Journal of Remote Sensing Journal Canadien De Télédétection **8**(2): 84-106.

Tian, J., L. Zhu and Y. Tang (2012). "Outdoor shadow detection by combining tricolor attenuation and intensity." Eurasip Journal on Advances in Signal Processing **2012**(1): 1-8.

Zhu, Z. and C. E. Woodcock (2012). "Object-based cloud and cloud shadow detection in Landsat imagery." Remote Sensing of Environment **118**(6): 83-94.